Breaking Down the Crystallinity: The Path for Advanced Lithium Batteries

*Chenxi Zu, Andrei Dolocan, Penghao Xiao, Shannon Stauffer, Graeme Henkelman, and Arumugam Manthiram**

Lithium-sulfur batteries offer high energy density, but their practical utility is plagued by the fast decay of lithium-metal anode upon cycling. To date, a fundamental understanding of the degradation mechanisms of lithium-metal anode is lacking. It is shown that (i) by employing a specifically designed electrolyte, the lithium-metal anode degradation can be significantly reduced, resulting in a superior, high-rate battery performance and (ii) by combining advanced, 3D chemical analysis with X-ray diffraction, the properties of the lithium-metal anode can be effectively monitored as a function of cycling, which is critical in understanding its degradation mechanisms. These findings suggest that the crystallinity of the impurity phases formed in the lithium-metal anode via chemical reactions with the electrolyte is the dominant degradation factor. It is shown both experimentally and by computational modeling that by employing electrolyte additives containing metal ions that have lower reactivity with sulfur than lithium (e.g., copper, silver, and gold), the crystallinity of the impurity phases can be significantly reduced, resulting in a stable lithium-metal anode. A pathway to develop a practical, affordable, environmentally compatible, rechargeable Li-S battery system is offered, and insights to develop other high-energy-density battery systems based on the high-capacity lithium-metal anode are provided.

1. Introduction

The global desire to replace polluting fossil fuels with clean renewable energy sources (e.g., solar, wind, hydro, and geothermal) requires efficient, reliable, low-cost electrical energy storage systems. In particular, the increasing consumption of fossil fuels by the transportation sector is prompting the development of advanced batteries for electric vehicles (EV).[1–15] As one of the most promising lithium-based batteries, the Li-S batteries are appealing as both the sulfur cathode and the lithium-metal anode offer an order of magnitude higher charge-storage capacity compared to the currently used insertion-compound electrodes.[16,17] In addition, sulfur is abundant and environmentally benign while lithium metal offers a desirable low negative electrochemical potential. Unfortunately, the lithium-metal anode suffers from nonuniform metal redeposition and unstable surface chemistry in organic electrolytes, which lead to a continuous breakdown and reformation of the solid electrolyte interphase (SEI) layer during cycling.[18] To stabilize the lithium-metal anode, various electrolyte systems that target the reduction of the amount of free solvent molecules causing unwanted side reactions have been proposed.[19–21] Stable high-rate performance with lithium-metal anode has been reported by employing electrolytes with high lithium-salt concentrations, but the practical application of these electrolyte systems in Li-S batteries has not been verified.[22] Alternatively, the concept of artificial SEI layers has been proposed, e.g., isolation of the lithium anode by hollow carbon nanosphere or lithiated graphite films.[23,24] Albeit increased cycling efficiency, the stability of the artificial SEIs in Li-S cells and their large-scale production remain a challenge for industrial applications.[25]

One key issue hampering the rational design of Li-S battery architecture is the limited understanding of the full chemical composition of the reacted lithium-metal anode and its connection to the structure and cell performance. Extensive studies employing X-ray photoelectron spectroscopy (XPS) and Fourier transform infrared spectroscopy (FTIR) have revealed the basic surface chemical composition of the reacted lithium-metal anodes.[26] The microstructure formation at the lithium-metal surface has also been investigated by optical microscopy,[27] secondary electron microscopy (SEM),[28] atomic force microscopy (AFM),[29] nuclear magnetic resonance (NMR) spectroscopy,[30] and hard X-ray microtomography.[31] To date, however, a clear correlation among the composition, long-range crystallinity and thickness of the reacted lithium region, and the cell performance has not been established.

Dr. C. Zu, Dr. A. Dolocan, Prof. A. Manthiram
Materials Science and Engineering Program
and Texas Materials Institute
The University of Texas at Austin
Austin, TX 78712, USA
E-mail: manth@austin.utexas.edu
Dr. P. Xiao, S. Stauffer, Prof. G. Henkelman
Department of Chemistry and the Institute for Computational Engineering and Sciences
The University of Texas at Austin
Austin, TX 78712, USA

DOI: 10.1002/aenm.201501933

Here, we present a methodology that combines time of flight secondary ion mass spectrometry (TOF-SIMS), SEM, and XRD to reveal the 3D chemical composition, morphology, and long-range crystallinity of the reacted lithium-metal anode that can be used to identify correlations between the materials characteristics and cell performance. With our methodology, we are able to determine the main degradation mechanism of lithium-metal anode, which allows for better cell design. In addition, we use first principles calculations to understand this degradation mechanism at the most fundamental level.

2. Results and Discussion

2.1. Advanced Cell Design

Our advanced Li-S cell is developed from the pristine cell through cathode engineering and anode modification (**Figure 1**a). The pristine cell combines a single-layer carbon nanofiber (CNF) current collector with polysulfide catholyte and a lithium-metal anode. To construct the sandwiched cell, the single-layer CNF current collector is replaced by two functional layers: the bottom CNF current collector designed to accommodate the polysulfide species and the upper composite current collector to control the sulfur species deposition (see the Experimental Section). We showed previously that a similar cathode modification could result in significant performance improvement.[32] For further design development, we start with the sandwiched cell configuration and modify the electrolyte with copper acetate additive (i.e., the advanced cell). The copper acetate additive was carefully chosen after identifying the best performance among other metallic (Ni, Fe, Cs, Ag, and Au) acetates (Figure S1, Supporting Information). After cycling, in contrast to the pristine cathode, which is characterized by larger domains of redeposited material, the sandwiched cathode exhibits a more uniform surface morphology, a result of the hydrophilic surface of the composite current collector (SEM images in Figure 1b,c).[32] On the anode side, for the

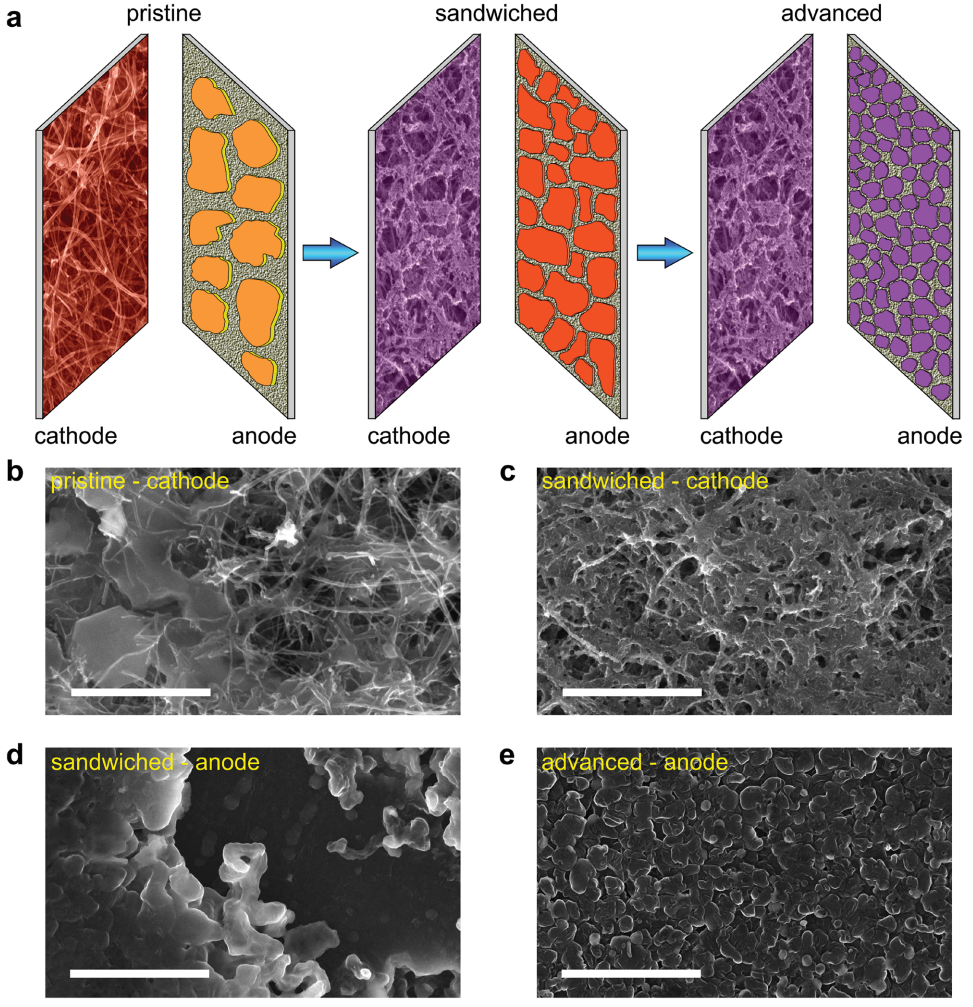

Figure 1. Cell development schematic. a) Schematic diagrams of the pristine, sandwiched, and advanced cells. The structure and morphology of the lithium anode evolve in different ways with various electrolytes, as discussed further in the text. SEM images of the b) cycled cathode in the pristine and c) sandwiched cells. SEM images of the d) cycled lithium-metal anode in the sandwiched and e) advanced cells. The cells were cycled at 1.0–3.0 V at C/2 (1 C = 1672 mA g^{-1}) for ten cycles. The scale bars in (b) and (c) are 10 μm; the scale bars in (d) and (e) are 50 μm.

sandwiched cell, lithium redeposition and stripping processes produce visible rod-like metal buildups and corrosion pits, in contrast to the advanced cell, which exhibits a more homogeneous surface morphology, implying a more controlled lithium-redeposition process (SEM images in Figure 1d,e).

2.2. Electrochemical Performance

It is known that the voltage hysteresis between charging and discharging of a battery is influenced by different electrochemical pathways.[33] Here, we define the value of this hysteresis to be the voltage difference between the middle of the charge (at half the maximum charge capacity) and discharge (at half the maximum discharge capacity) curves (**Figure 2**a). For the advanced cell, the upper and lower plateaus of the discharge curves for the 10th and 100th cycle overlap, indicating a stable passivation layer (Figure 2a). Additionally, the advanced cell exhibits the lowest hysteresis (Figure 2b) and most stable Coulombic efficiency (Figure 2c) throughout 150 cycles, among all cells, demonstrating better reversibility and stability. After prolonged cycling for 150 cycles at C/2 discharge rate, in contrast to the pristine cell which retains <10% of its initial capacity, the advanced cell displays a capacity retention of 60% (i.e., 808 mAh g^{-1}) (Figure 2d). Moreover, the advanced cell retains a reversible capacity of 450 mAh g^{-1} at 1C rate after 250 cycles (Figure S2, Supporting Information). To our knowledge, this is the best performance reported at comparable sulfur content (loading of 5 mg cm^{-2}) and discharge rates, proving the advantages of our advanced cell for meeting the energy requirements of EVs.

2.3. Morphology and 3D Chemical Analysis

To understand the superior performance of the advanced cell, we focus our study on the evolution of the lithium-metal anode during cycling, which has been previously demonstrated to be the main limiting factor.[32,34] We use TOF-SIMS to investigate the 3D chemical composition of the lithium anode surface with the purpose of revealing the SEI layer composition and the role of copper and sulfur in lithium redeposition.

Figure 3a presents the TOF-SIMS depth profiles of the lithium anodes in the sandwiched and advanced cells after the first cycle. The C^- and S^- profiles show (i) a large depth penetration (>10 µm), suggesting that the electrolyte both reacts with the Li anode and serves as a transport medium for the various species (e.g., sulfur) that react with the Li anode during cycling (i.e., the reacted lithium region), and (ii) a higher intensity for the sandwiched cell, indicating a higher amount of diffused electrolyte. As a result of electrolyte decomposition, carbon sulfide species (represented by the CS^- marker) form at the very surface of the Li anode, with a thickness estimated at ≈300 nm for the advanced cell and ≈170 nm for the sandwiched cell (Figure 3a, green curves). This top layer also contains higher amounts of lithium sulfide species, $Li_xS_{(1-x)}$ (where $0 < x < 1$, represented by the LiS^- marker), in the sandwiched

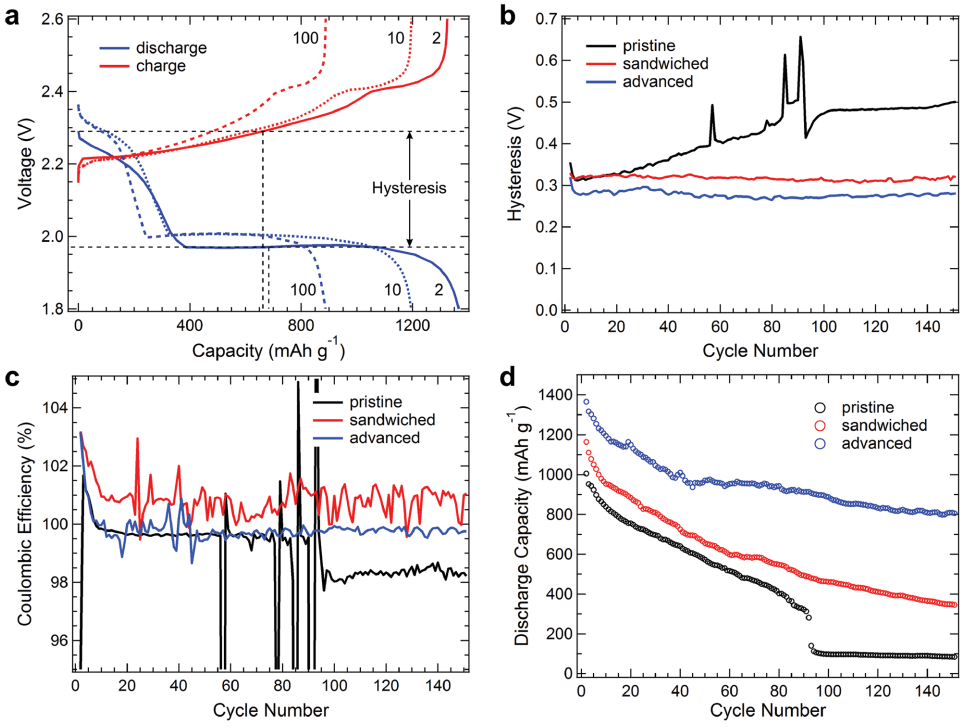

Figure 2. a) Charge and discharge curves of the advanced cell. The charge rate is C/10 and the discharge rate is C/2. b) Voltage hysteresis of the pristine, sandwiched, and advanced cells. c) Coulombic efficiencies of the pristine, sandwiched, and advanced cells. The ratio between the discharge and charge capacities defines the Coulombic efficiency. d) Cycling performances at C/10-charge rate and C/2-discharge rate for the pristine, sandwiched, and advanced cells. The cells were characterized between 1.8 and 2.6 V.

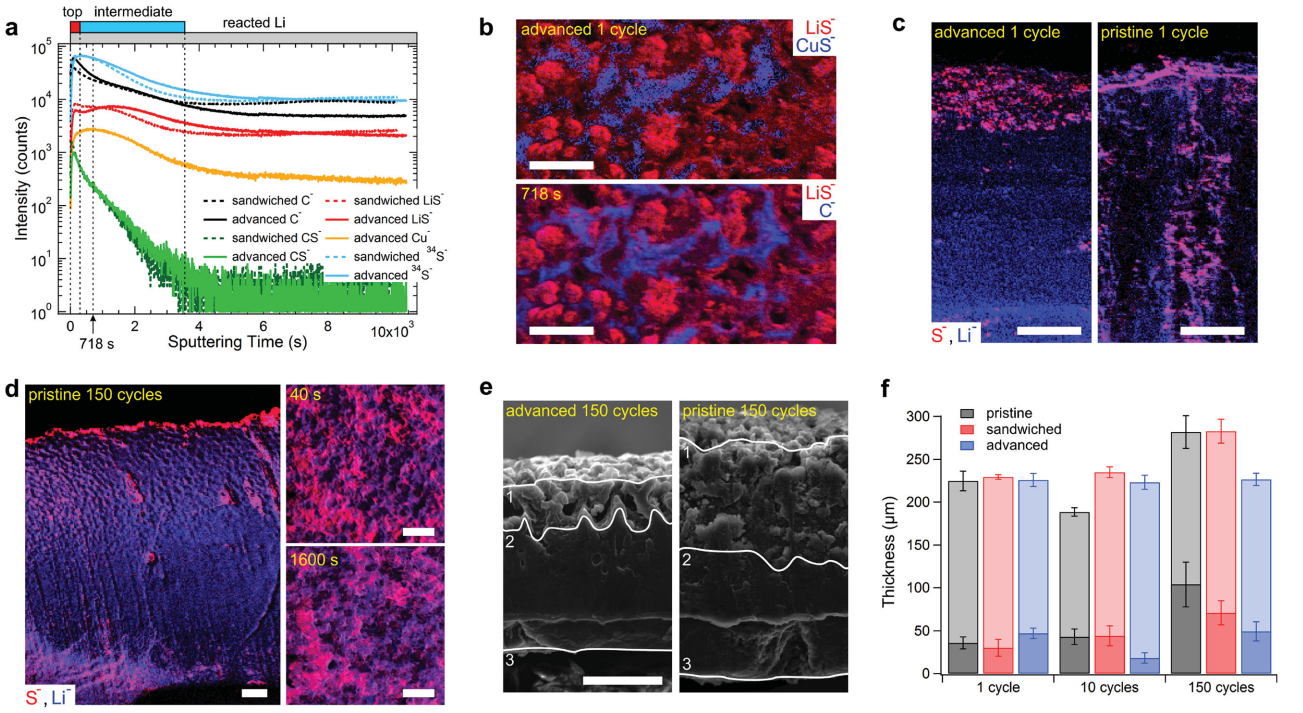

Figure 3. Chemical and morphological analysis. a) Comparative TOF-SIMS depth profiles of lithium anodes of the advanced and sandwiched cells after the first cycle. b) TOF-SIMS chemical mapping showing the overlay of LiS^- and CuS^- species (LiS^- in red and CuS^- in blue) and of LiS^- and C^- species (LiS^- in red and C^- in blue) at the surface of the cycled lithium anode of the advanced cell after 718 s Cs^+ sputtering, as indicated in (a). c) TOF-SIMS cross-sectional chemical mapping showing the overlay of S^- and Li^- species (S^- in red and Li^- in blue) in the lithium anodes of the advanced cell and the pristine cell after the first cycle. d) TOF-SIMS cross-sectional (left) and surface (right) chemical mapping showing the overlay of S^- and Li^- species (S^- in red and Li^- in blue) in the lithium anode of the pristine cell after 150 cycles. The surface mappings (right) are acquired after 40 and 1600 s Cs^+ sputtering. e) Cross-sectional SEM imaging of the lithium anodes of the advanced and pristine cells after 150 cycles. f) Statistical analysis of the anode (lighter colors) and reacted lithium (darker colors) regions thickness for the pristine, sandwiched, and advanced cells. The scale bars in (b–d) are 20 μm; the scale bar in (e) is 100 μm.

cell compared to the advanced cell, one of the possible reasons for the lower lithium activity in the sandwiched cell. Following the top layer, an intermediate region, extending up to ≈4 μm in depth, exhibits a significant depth separation between the maxima of the Cu^- and LiS^- profiles in the case of the advanced cell, suggesting that the Cu compounds formed during cycling change the distribution of the lithium sulfide species in this layer by inhibiting their formation. Additional evidence of suppression of $Li_xS_{(1-x)}$ formation by Cu is inferred from Figure 3b, which shows different lateral distributions of two typical Cu and Li reacted species (represented by CuS^- and LiS^-, respectively) after 718 s of Cs^+ sputtering. Representing the electrolyte, the carbon-related species (indicated by the C^- marker) exhibit an identical lateral distribution with the copper sulfide species, implying that the electrolyte is responsible for the copper transport in the lithium matrix.

A comparative cross-sectional TOF-SIMS high-resolution mapping for the advanced and pristine cells after the first cycle is shown in Figure 3c. The different sulfur distribution (displayed in red) in the reacted lithium region for the two cells suggests different sulfur reaction pathways. We observe significantly more $Li_xS_{(1-x)}$ species (i.e., the purple color, a result of the overlap of the Li^-, in blue, and S^-, in red, secondary ions) in the pristine cell, mostly accumulated at the surface, whereas the sulfur appears discretely distributed in the lithium reacted region of the advanced cell, implying less local strain/stress that should lead to a more stable SEI.

TOF-SIMS elemental mappings of a cross section (Figure 3d, left image) and surface (Figure 3d, right images) of a pristine cell after 150 cycles provide insight into the fading mechanism of lithium-metal anode. An obvious sulfur-rich layer (≈2–5 μm) is formed at the surface during prolonged cycling (left image), presenting a discontinuous planar but a compact depth distribution (right images). Suggested by its granular texture, the reacted lithium region (>100 μm) appears composed of pulverized lithium particles coated with sulfur, indicating significant parasitic side reactions between lithium-metal and the electrolyte. In agreement with the TOF-SIMS results in Figure 3d, cross-sectional SEM imaging shows both a substantial thickness increase and pulverization of the lithium-reacted region (defined by the curves 1 and 2 in Figure 3e) for the pristine cell (>100 μm) compared to the advanced cell after prolonged cycling (i.e., 150 cycles). The statistical analysis of the lithium anodes for all three cells based on cross-sectional SEM imaging (Figure 3f) reveals (i) a continuous increase in the anode thickness (defined by the curves 1 and 3) and the lithium-reacted region in both the pristine and sandwiched cells, and (ii) a relatively constant thickness of the lithium anode and lithium-reacted region in the advanced cell, with cycling. It appears that the increase in the anode thickness for the pristine and

sandwiched cells is a result of the increasing lithium-reacted region. Given the measured thicknesses of the lithium-reacted regions (Figure 3f) and the corresponding discharge capacities (Figure 2d), we calculate that after prolonged cycling (i.e., >150 cycles), only a fraction of the lithium mass contained in the reacted-lithium region (Figure S3, Supporting Information) participates in the cycling process, with the advanced cell showing the highest efficiency of lithium usage (≈40%) and the pristine cell the lowest (<2%). For the advanced cell, the thickness of the lithium reacted region decreases after the first cycle due to the electrochemical activation/conditioning in the following cycles that leads to the redistribution of the SEI.[12]

2.4. Structural and Electrochemical Properties

Upon cycling, the structure of lithium anode can evolve significantly. These changes can be investigated by XRD, as shown in **Figure 4**a,b. After 150 cycles, in contrast to the advanced cell where only the crystalline lithium peaks are visible, the pristine and sandwiched cells exhibit additional peaks that correspond to LiOH (PDF #01-085-0736) and Li_2S (PDF #01-077-2874) crystalline phases, respectively (Figure 4a). To relatively quantify, between different cells, the amount of crystalline impurity phases appearing in the lithium anode, we define SEI crystallinity as the ratio between the total area of all XRD peaks other than lithium and the total area of lithium peaks (Note S1, Supporting Information). Such defined, for a given cell, the SEI crystallinity compensates for the variations in the X-ray intensity and is directly proportional to the absolute amount of the crystalline impurities contained in the lithium anode, thus allowing for a direct comparison of this amount between different cells. For both the pristine and sandwiched cells, the SEI crystallinity increases significantly with cycling (Figure 4b) due to the growth of LiOH and Li_2S crystalline impurity phases at the lithium grain boundaries,[35] leading to the expansion of the anode, as observed in Figure 3f. In contrast, the SEI crystallinity of the advanced cell is decreasing substantially, indicating the different chemistry during cycling. For the advanced cell, we think the copper acetate is actively reducing the long-range crystallinity of the SEI impurity phases in the reacted lithium region, thus increasing the lithium-ion conductivity compared to that in the pristine and sandwiched cells, which might explain the lower hysteresis and superior battery performance of the advanced cell. The XRD patterns of the pristine and sandwiched cells after they were assembled and left uncycled for 48 h (i.e., resting; Figure 4b) suggest the crystallinity of the lithium-reacted region is predominantly originating from pure chemical processes. In contrast, the advanced cell shows no SEI crystallinity both after resting or long-term cycling (>150 cycles), which implies that neither chemical nor electrochemical processes generate long-range crystallinity in the resulting SEI impurity phases. For all the cells, after short-term cycling (i.e., approximately few tens of cycles), the crystallinity of the reacted-lithium region can be composed of both Li_2S and LiOH phases (Table S1, Supporting Information). After cycling for 150 cycles, in contrast to the sandwiched cell, the pristine cell shows SEI crystallinity rich in LiOH phase, indicating a

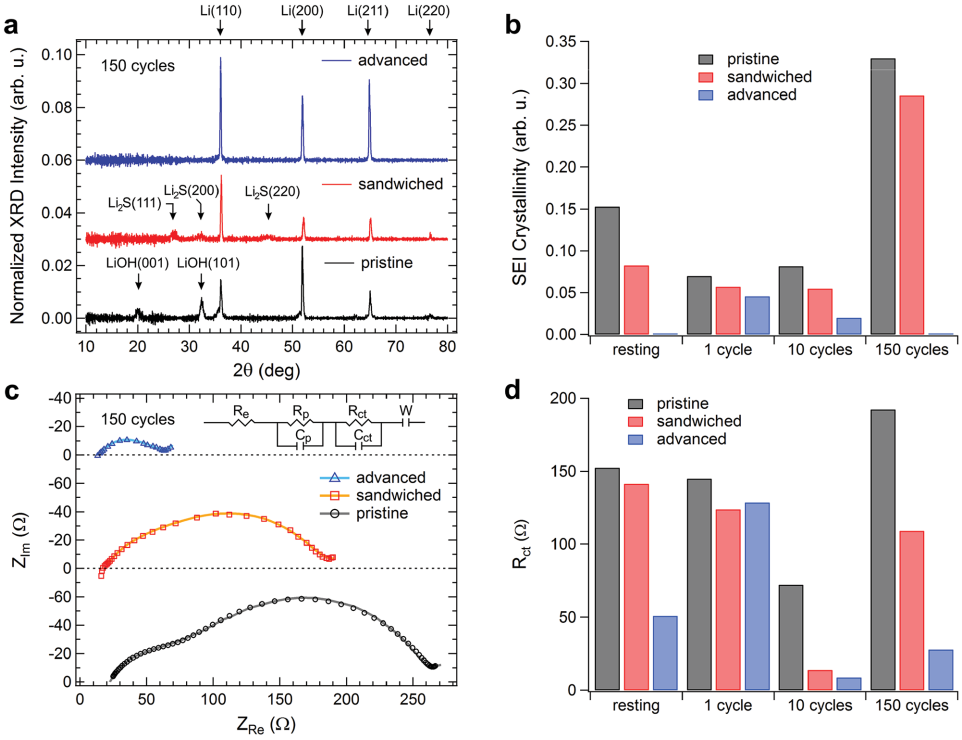

Figure 4. Structural and electrochemical properties. a) XRD patterns for the lithium anodes of pristine, sandwiched, and advanced cells after 150 cycles. All patterns have the background subtracted. b) Variation of the lithium anode SEI crystallinity between different cells. c) EIS spectra for the pristine, sandwiched, and advanced cells after 150 cycles. d) R_{ct} variation between different cells.

more severe side reaction between lithium-metal anode and electrolyte solvent rather than the polysulfide species.

Electrochemical impedance spectroscopy (EIS) was performed to characterize the electrochemical properties of the cells (Figure 4c). The specific EIS curves were fitted according to the equivalent circuit presented in Figure 4c (inset), with the values of the equivalent circuit elements listed in Table S2 (Supporting Information). In general, the charge-transfer resistance R_{ct} decreases during the initial stages of cycling due to the electrochemical conditioning (e.g., redistribution of the polysulfide species to allow for better electrochemical contact), but increases when resting or during long-term cycling due to the electrode degradation. R_{ct} of the pristine cell is the highest in each individual cycle indicating the most difficult electrochemical charge-transfer process. An increase in SEI crystallinity could result in a more difficult accommodation of Li^+ ions at the Li/SEI interface,[36] which could explain the more difficult electrochemical charge transfer. According to Table S2 (Supporting Information), the small interphase contact resistance R_p in the advanced cell confirms the slower growth of an insulating electrode passivation with cycling. In addition, we notice that the electrolyte resistance R_e maintains a low and roughly constant value for the advanced cell, in contrast to the pristine and sandwiched cells, indicating a significantly lower consumption of the electrolyte during cycling. The lower electrolyte depletion in the advanced cell is confirmed by both the lower C^- signal in the Li anode bulk (Figure 3a) and the thinner Li reacted region (Figure 3f).

2.5. Computational Modeling

In order to understand the influence of Cu on the stability and growth of $Li_xS_{(1-x)}$ phases, we employ density functional theory (DFT) calculations to examine the relative stability of the $Li_xS_{(1-x)}$ bulk phases in the absence or presence of Cu (**Figure 5**a,b). At each composition x, we use a basin-hopping simulation to determine the most stable $Li_xS_{(1-x)}$ structure based on the minimum formation energy.[37] The super-cell representing the material is chosen to be sufficiently large to properly capture both crystalline and amorphous structures. In the absence of Cu, only Li_2S is found to have a crystalline structure as the global minimum, while all the other investigated compositions exhibit amorphous ground states (Figure 5a). The convex hull (Figure 5a, blue line) represents the lowest possible formation energy for a given composition and shows Li_2S as the only stable intermediate. Consequently, any other amorphous $Li_xS_{(1-x)}$ structure will thermodynamically decompose into the crystalline Li_2S phase, which explains the significant amount of Li_2S appearing at the pristine and sandwiched anodes. Given that for the advanced cell, in the presence of Cu, TOF-SIMS identifies a phase separation between CuS^- rich and LiS^- rich regions (Figure 3b), we expect such a CuS-phase to change the relative stability of the supported Li_2S crystalline phase as compared to other $Li_xS_{(1-x)}$ amorphous phases. To test this hypothesis, we employ a model system with a crystalline CuS(001) substrate to calculate a Cu-modified $Li_xS_{(1-x)}$ convex hull (Figure 5b, blue line). The two end points, pure Li and S, are also supported on CuS(001) to give proper reference energies. Surprisingly, in the presence of CuS, all of the amorphous $Li_xS_{(1-x)}$ structures are on, or very close to the hull, as shown in Figure 5b. Moreover, when S exceeds 0.4 in composition, which is reasonable at the electrolyte-anode boundary, the formation of Li_2S is thermodynamically unfavorable. Instead, a new, amorphous phase, $Li_{1.5}S$, emerges as the most stable structure, indicating a stabilized growth of S-rich amorphous phases in the presence of the CuS phase.

The diffusivity of Li can be estimated by the energy required to create the point defects that carry Li in the different phases. In the crystalline phase Li_2S, the vacancy and interstitial formation energies equate 3.4 and 1.5 eV, respectively, implying a slow Li transport. On the other hand, the interstitial formation energy for amorphous $Li_xS_{(1-x)}$ structures increases with Li concentration from −1.2 eV for LiS_2 to −1 eV for $Li_{1.5}S$, and is expected to cross 0 eV before reaching the Li_2S composition, thus indicating that the amorphous phases could support Li interstitials and are more likely to transport Li than the crystalline Li_2S, which explains the higher Li-ion conductivity of the advanced cell.

The inverse proportionality between cell performance and SEI crystallinity is verified for the pristine cell by modifying its configuration with electrolyte additives composed of various metal (Fe, Ni, Cu, Ag, Cs, and Au) acetates (Figure 5c). A higher Gibbs free energy of reaction between the metal ions and sulfur (i.e., a lower reactivity with sulfur, e.g., Cu, Ag, Au; Table S3, Supporting Information) is found to decrease the SEI crystallinity (Table S4, Supporting Information), a result of the additive-induced passivation that likely reduces the anode chemical reactivity with sulfur. We expect a similar reduction of lithium reactivity toward oxygen and carbon when using additives containing metal ions from the platinum and gold groups (Tables S5 and S6, Supporting Information). As indicated in our theoretical model, these select metal ions inhibit the crystalline phase formation of the impurities at the lithium grain boundaries by actively changing their surface energy. Other factors such as solvation and ionic mobility may also influence the passivation effects of the additives. During operation, the lithium ions in the SEI or close to the lithium grain boundaries are likely extracted and redeposited (together with other impurity phases) through the SEI (Figure 5d), which explains the large influence the SEI crystallinity has on cell performance.

3. Conclusion

To summarize, we demonstrate the subtle differences in chemical composition between various cell designs employing TOF-SIMS, an ultrahigh surface sensitive technique that can provide full, 3D chemical mapping of the reacted lithium region.[38,39] In conjunction with XRD, TOF-SIMS and SEM imaging indicate the main degradation mechanisms of lithium anodes in Li-S batteries: the continuous growth of redeposited impurity phases with long-range crystallinity in the SEI layer. A solution is identified: electrolyte additives containing metal ions having lower reactivity with sulfur than lithium (e.g., Cu, Ag, Au), capable of inhibiting the long-range crystallinity of the redeposited impurity phases and the passivation layer growth. Our first principles theoretical model indicates the fundamental mechanism

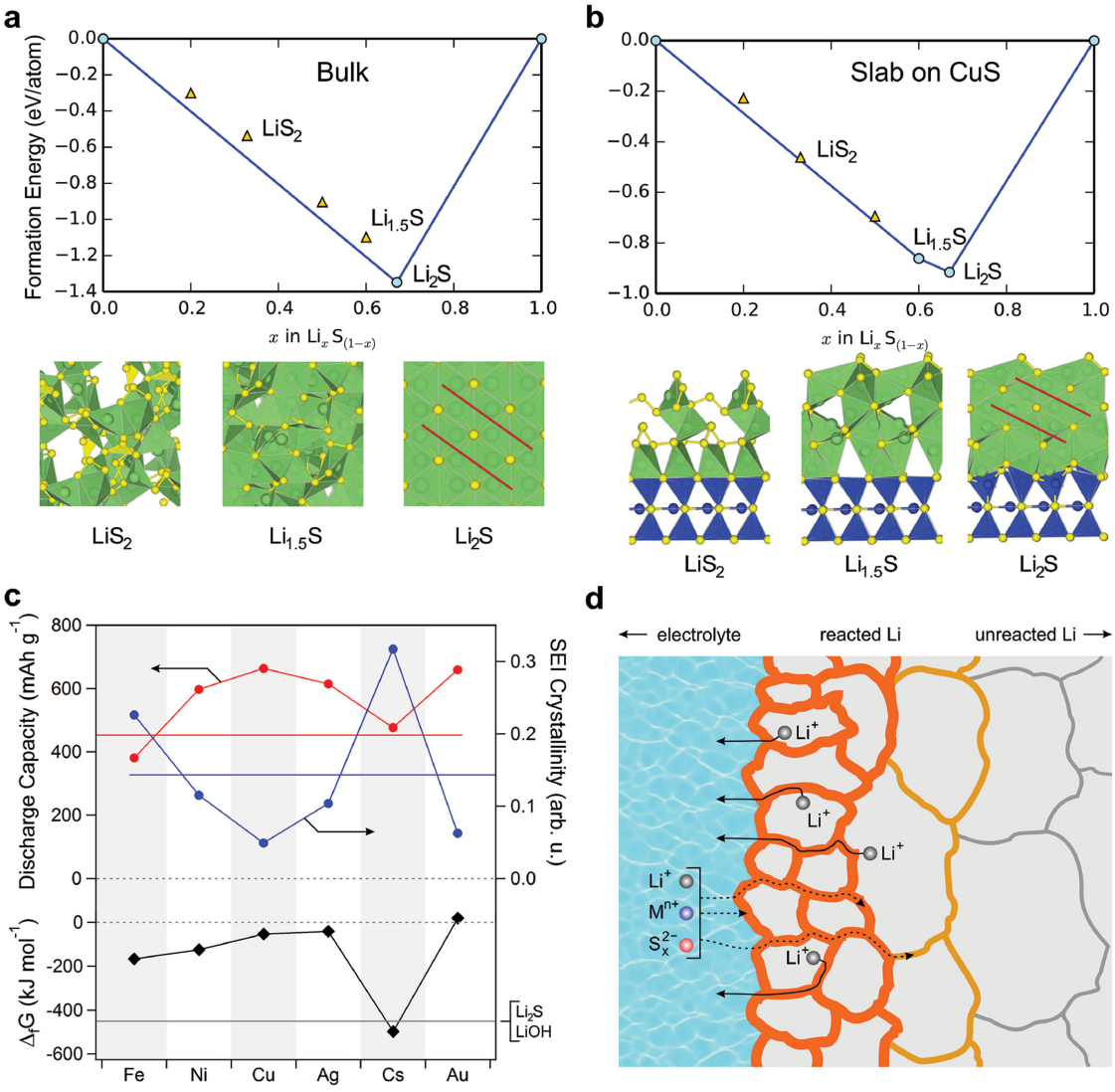

Figure 5. Computational modeling. Convex hulls of stability for a) bulk $Li_xS_{(1-x)}$ and b) a layer of $Li_xS_{(1-x)}$ supported on a CuS(001) substrate. The circles (on the hull) and triangles (above the hull) represent the stable and unstable phases, respectively. Selected structures composed of Li (green), S (yellow), and Cu (blue) atoms are shown below. The red lines on the Li_2S structures indicate the (111) crystalline planes. c) The correlation between the discharge capacities after 30 cycles and SEI crystallinities of the pristine cell following the electrolyte modification with various metal acetates. The discharge capacity and SEI crystallinity of the pristine cell without any electrolyte modifications are shown as the red and blue horizontal lines, respectively. A lower reactivity with sulfur (i.e., a higher Gibbs free energy of reaction) of the metal additives reduces the formation of lithium polysulfide species by reducing the surface reactivity of the lithium anode with sulfur. The Gibbs free energy of reaction of Li_2S and LiOH are displayed as the dark gray horizontal line. d) Schematic representation of lithium-ion extraction and redeposition pathways during cycling.

of the suppression of crystallinity and predicts the higher Li-ion conductivity in amorphous, S-rich LiS structures. Future work focused on reducing the long-range crystallinity of the redeposited impurity phases at the lithium-metal anode is expected to further improve the performance of lithium-based batteries. Application of our analytical approach to these systems could further enhance the fundamental understanding of the interaction between the electrolyte and lithium-metal anode, which could lead to better design of lithium- or, in general, metal-based battery architectures and their mass-production capabilities.

4. Experimental Section

Synthesis of CNF Current Collector and Composite Current Collector: To synthesize CNF current collector, carbon nanofibers (90–150 mg, Fisher Scientific) were dispersed in de-ionized water (700 mL) and isopropyl alcohol (50 mL), ultrasonicated for 15 min, and vacuum filtrated to produce the free-standing CNF film. In order to prepare the composite current collector, carbon nanofibers (120 mg), Ketjenblack carbon nanopowders (40 mg, Akzo Nobel), sodium alginate (10 mg, Fisher Scientific), and polyvinyl alcohol (10 mg, Fisher Scientific) were first suspended in a miscible solution of water (100 mL) and isopropyl

alcohol (100 mL) to prepare a slurry. The slurry was poured into a surface-cleaned glass petri dish and naturally aged at room temperature until the obtained composite film can be easily peeled off, which further decreased the thickness of the composite film to <10 μm (i.e., modified gelation strategy). The CNF film and composite film were then cut into circular electrode of 0.64 cm in diameter. The thickness of the CNF current collector is ≈100 μm.

Synthesis of Electrolyte and Polysulfide Catholyte: $LiCF_3SO_3$ (98%, Acros Organics, 1 M) in 1,2-dimethoxyethane (DME, 99+%, Acros Organics) and 1,3-dioxolane (DOL, 99+%, Acros Organics) (1:1 ratio, by volume) constitutes the blank electrolyte. The blank electrolyte was used to dissolve sublimed sulfur (99+%, Fisher Scientific) and Li_2S (99+%, Acros Organics) (5:1 ratio, by mole) to produce the catholyte with the main composition of Li_2S_6 (0.5 M). On the other hand, the anolyte for the pristine, sandwiched cell, and advanced cell had $LiNO_3$ (99+%, Acros Organics, 1 M) in the blank electrolyte, whereas anhydrous metallic acetate (0.06 M, 99+%, Fisher Scientific) was further added into the anolyte that was introduced into the advanced cell.

Electrochemical Test: CR2032 coin cells were assembled in an argon-filled glove box for electrochemical characterization. The pristine cell contained one-single-layer CNF current collector, while the sandwiched cell and advanced cell each had a CNF bottom current collector and a composite upper current collector. Polysulfide catholyte was sandwiched between the two current collectors before adding the Celgard 2400 separator, anolyte, and the lithium-metal anode. The sulfur content was controlled to be ≈55 wt% in the free-standing cathodes in the pristine cell, sandwiched cell, and advanced cell. The sulfur loading is ≈5 mg cm^{-2}. No metal current collector was needed.

Galvanostatic cycling was conducted at room temperature with an Arbin battery cycler at 1.0–3.0 or 1.8–2.6 V (vs Li/Li^+). The specific discharge capacity was calculated based on the mass of sulfur. The initial discharge curve of the advanced cell is shown in Figure S4 (Supporting Information). EIS measurements were performed with an impedance analyzer (Solartron 1260 A) in the frequency range of 1 MHz to 0.1 Hz with an AC voltage amplitude of 5 mV at the OCV. The cells were charged to 2.6 V before characterization. CV profiles were obtained with a VoltaLab PGZ 402 Potentiostat. To study the function of metal-containing additives on the morphologies of the lithium anode in electrolyte without polysulfides, lithium deposition study was also performed with details shown in Notes S2 and S3 (Supporting Information).

Materials Characterization: The crystalline phase of the prepared lithium-metal anode was identified at several stages during cycling by X-ray diffraction (Rikagu MiniFlex 600) with CuKα radiation (λ = 1.54184 Å). The XRD signal was detected for diffraction angles (2θ) between 10° and 80° at a scan rate of 0.03° s^{-1}. Kapton film was used to protect the lithium-metal anode from air. The XRD patterns shown in paper have the Kapton film background (Figure S5, Supporting Information) subtracted. Morphologies of the electrodes were examined by SEM (FEI Quanta 650 ESEM) equipped with a Bruker EDX system. The cross sections were prepared inside a glove box (argon environment) by mechanical cutting.

TOF-SIMS Characterization: A time-of-flight secondary ion mass spectrometer (TOF.SIMS 5 by ION-TOF GmbH, 2010) was used for chemical analysis of the lithium-metal anodes. The data were acquired with the analysis ion beam (Bi_1^+, 30 keV ion energy) set in either the high current (HC) mode (≈3 pA measured sample current) for depth profiling or burst alignment (BA) mode (≈0.4 pA measured sample current) for high lateral resolution mapping (<200 nm) of the species of interest at the surface or in the cross section of the cycled anodes. The analyzed area, typically 100 × 100 μm^2, was raster scanned at 256 × 256 pixels in both modes. A sputtering ion beam (Cs^+ with 2 keV ion energy and ≈70 nA measured sample current) was used for depth profiling (250 × 250 μm^2 sputtered area, centered on the analysis area) and shallow milling of the cross sections to reduce possible contamination when performing high-resolution mapping. The sputtering rate of lithium by the Cs^+ beam was estimated to be ≈1 nm s^{-1} (Figure S6, Supporting Information). All detected secondary ions had negative polarity. The mass resolution ($m/\delta m$) in HC mode was >5000 while in BA mode was <100. The experiments were performed in ultrahigh vacuum (UHV) at a base pressure of $<10^{-9}$ mbar. All samples were transferred from the preparation glove box to the TOF-SIMS analysis chamber in an air-free environment.

Theoretical Model: All energies were calculated by DFT with the PBE functional for the exchange correlation energy as implemented in the Vienna ab initio simulation package (VASP).[40,41] The PAW potentials were employed to account for the core electrons.[42,43] A plane wave basis set with an energy cutoff of 384 eV was used to model the valence electrons. Global optimizations were performed with the basin-hopping algorithm. For the CuS substrate, the bottom two layers of CuS were fixed in their bulk crystalline positions, while the top layer was allowed to relax along with the supported $Li_xS_{(1-x)}$ compounds.

Supporting Information

Supporting Information is available from the Wiley Online Library or from the author.

Acknowledgements

C.Z. and A.D. contributed equally to this work. This work was supported by the U.S. Department of Energy, Office of Basic Energy Sciences, Division of Materials Sciences and Engineering under Award No. DE-SC0005397. The authors also acknowledge the National Science Foundation grant DMR-0923096 for the acquisition of the TOF-SIMS instrument, as part of the Texas Materials Institute at the University of Texas at Austin.

Received: September 26, 2015
Revised: November 6, 2015
Published online: December 17, 2015

[1] R. Van Noorden, *Nature* **2014**, *507*, 26.
[2] a) P. G. Bruce, L. J. Hardwick, K. M. Abraham, *MRS Bull.* **2011**, *36*, 506; b) L. Grande, E. Paillard, J. Hassoun, J.-B. Park, Y.-J. Lee, Y.-K. Sun, S. Passerini, B. Scrosati, *Adv. Mater.* **2015**, *27*, 784.
[3] C. Zu, H. Li, *Energy Environ. Sci.* **2011**, *4*, 2614.
[4] Y. Lu, Z. Tu, L. A. Archer, *Nat. Mater.* **2014**, *13*, 961.
[5] Y. Xu, Y. Wen, Y. Zhu, K. Gaskell, K. A. Cychosz, B. Eichhorn, K. Xu, C. Wang, *Adv. Funct. Mater.* **2015**, *25*, 4312.
[6] G. M. Zhou, F. Li, H. M. Cheng, *Energy Environ. Sci.* **2014**, *7*, 1307.
[7] Z. Wang, L. Zhou, X. W. Lou, *Adv. Mater.* **2012**, *24*, 1903.
[8] Z. Li, L. Yuan, Z. Yi, Y. Sun, Y. Liu, Y. Jiang, Y. Shen, Y. Xin, Z. Zhang, Y. Huang, *Adv. Energy Mater.* **2014**, *4*, 1301473.
[9] R. Xu, J. Lu, K. Amine, *Adv. Energy Mater.* **2015**, *5*, 1500408.
[10] H. J. Peng, J. Q. Huang, M. Q. Zhao, Q. Zhang, X. B. Cheng, X. Y. Liu, W. Z. Qian, F. Wei, *Adv. Funct. Mater.* **2014**, *24*, 2772.
[11] Y. Qiu, G. Rong, J. Yang, G. Li, S. Ma, X. Wang, Z. Pan, Y. Hou, M. Liu, F. Ye, W. Li, Z. W. Seh, X. Tao, H. Yao, N. Liu, R. Zhang, G. Zhou, J. Wang, S. Fan, Y. Cui, Y. Zhang, *Adv. Energy Mater.* **2015**, DOI: 10.1002/aenm.201501369.
[12] S.-E. Cheon, K.-S. Ko, J.-H. Cho, S.-W. Kim, E.-Y. Chin, H.-T. Kim, *J. Electrochem. Soc.* **2003**, *150*, A800.
[13] A. Manthiram, Y. Fu, S.-H. Chung, C. Zu, Y.-S. Su, *Chem. Rev.* **2014**, *114*, 11751.
[14] A. Manthiram, S.-H. Chung, C. Zu, *Adv. Mater.* **2015**, *27*, 1980.
[15] J. B. Goodenough, Y. Kim, *Chem. Mater.* **2010**, *22*, 587.
[16] Y. Yang, G. Zheng, S. Misra, J. Nelson, M. F. Toney, Y. Cui, *J. Am. Chem. Soc.* **2012**, *134*, 15387.

[17] S. Evers, L. F. Nazar, *Acc. Chem. Res.* **2013**, *46*, 1135.
[18] E. Peled, *J. Electrochem. Soc.* **1979**, *126*, 2047.
[19] S. Zhang, K. Ueno, K. Dokko, M. Watanabe, *Adv. Energy Mater.* **2015**, *5*, 1500110.
[20] W. Xu, J. Wang, F. Ding, X. Chen, E. Nasybulin, Y. Zhang, J.-G. Zhang, *Energy Environ. Sci.* **2014**, *7*, 513.
[21] L. Suo, Y.-S. Hu, H. Li, M. Armand, L. Chen, *Nat. Commun.* **2013**, *4*, 1481.
[22] J. Qian, W. A. Henderson, W. Xu, P. Bhattacharya, M. Engelhard, O. Borodin, J.-G. Zhang, *Nat. Commun.* **2015**, *6*, 6362.
[23] G. Zheng, S. W. Lee, Z. Liang, H.-W. Lee, K. Yan, H. Yao, H. Wang, W. Li, S. Chu, Y. Cui, *Nat. Nano technol.* **2014**, *9*, 618.
[24] C. Huang, J. Xiao, Y. Shao, J. Zheng, W. D. Bennett, D. P. Lu, L. V. Saraf, M. Engelhard, L. Ji, J.-G. Zhang, X. Li, G. L. Graff, L. Liu, *Nat. Commun.* **2014**, *5*, 3015.
[25] R. Bouchet, *Nat. Nano technol.* **2014**, *9*, 572.
[26] D. Aurbach, E. Pollak, R. Elazari, G. Salitra, C. S. Kelley, J. Affinito, *J. Electrochem. Soc.* **2009**, *156*, A694.
[27] C. Brissot, M. Rosso, J.-N. Chazalviel, S. Lascaud, *J. Electrochem. Soc.* **1999**, *146*, 4393.
[28] M. Dolle, L. Sannier, B. Beaudoin, M. Trentin, J. M. Tarascon, *Electrochem. Solid State* **2002**, *5*, A286.
[29] D. Aurbach, Y. Cohen, *J. Electrochem. Soc.* **1996**, *143*, 3525.
[30] R. Bhattacharyya, B. Key, H. Chen, A. S. Best, A. F. Hollenkamp, C. P. Grey, *Nat. Mater.* **2010**, *9*, 504.
[31] K. J. Harry, D. T. Hallinan, D. Y. Parkinson, A. A. MacDowell, N. P. Balsara, *Nat. Mater.* **2014**, *13*, 69.
[32] C. Zu, A. Manthiram, *Adv. Energy Mater.* **2014**, *4*, 1400897.
[33] M. Cuisinier, P. E. Cabelguen, S. Evers, G. He, M. Kolbeck, A. Garsuch, T. Bolin, M. Balasubramanian, L. F. Nazar, *J. Phys. Chem. Lett.* **2013**, *4*, 3227.
[34] C. Zu, A. Manthiram, *J. Phys. Chem. Lett.* **2014**, *5*, 2522.
[35] K. Morigaki, A. Ohta, *J. Power Sources* **1998**, *76*, 159.
[36] F. M. Delnick, *J. Power Sources* **1989**, *26*, 129.
[37] D. J. Wales, J. P. K. Doye, *J. Phys. Chem. A* **1997**, *101*, 5111.
[38] H. Chou, A. Ismach, R. Ghosh, R. S. Ruoff, A. Dolocan, *Nat. Commun.* **2015**, *6*, 7482.
[39] T. D. M. Elko-Hansen, A. Dolocan, J. G. Ekerdt, *J. Phys. Chem. Lett.* **2014**, *5*, 1091.
[40] G. Kresse, J. Hafner, *Phys. Rev. B* **1993**, *47*, R558.
[41] J. P. Perdew, K. Burke, M. Ernzerhof, *Phys. Rev. Lett.* **1996**, *77*, 3865.
[42] P. E. Blöchl, *Phys. Rev. B* **1994**, *50*, 17953.
[43] G. Kresse, D. Joubert, *Phys. Rev. B* **1999**, *59*, 1758.

